WILEY | Hindawi

Research Article

Highly Semiconducting One-Dimensional Porous ZnO Nanorod Array Nanogenerators for Mechanical Energy Harvesting Functions

Dong Jin Lee,[1] **Ganesan Mohan Kumar,**[1] **Deuk Young Kim,**[1,2] **and Pugazhendi Ilanchezhiyan** [1]

[1]*Quantum-Functional Semiconductor Research Center (QSRC), Institute of Future Technology, Dongguk University-Seoul, Seoul, Republic of Korea*
[2]*Division of Physics and Semiconductor Science, Dongguk University-Seoul, Seoul, Republic of Korea*

Correspondence should be addressed to Pugazhendi Ilanchezhiyan; ilancheziyan@dongguk.edu

The development of energy harvesters based on inexpensive inorganic materials has attracted considerable attention to envisage next-generation self-powered electronic devices. In this work, we presented surface modification of ZnO nanorods (NRs) by thermochemical reaction using photoresist (PR) as an etching source. The morphological and microstructural properties of surface-etched ZnO NRs (M: ZnO) were systematically studied in detail through SEM and HRTEM. The morphological results show that the surface-etched NRs possess nanofiber-like porous structures and are penetrated throughout the NRs with high surface area. We fabricated triboelectric nanogenerators (TENG) using M: ZnO NRs with poly (dimethylsiloxane) (PDMS) as negative triboelectric material and mica as positive triboelectric material. The prepared M: ZnO NR TENG successfully delivered an output voltage of up to 20 V and a current density of $3.2\,\mu A\,cm^{-2}$, which is ~1.5 times higher than those observed for smooth ZnO NRs, respectively. The prepared M: ZnO NR TENG device can be able to lit 24 red light-emitting diodes (LEDs) as the power source. Finally, to demonstrate the practical applications of M: ZnO NR TENG, it was attached to the human body (elbow, knee, wrist, and heel) and efficiently harvested the energy from daily human activities.

1. Introduction

In recent years, developing and searching for renewable, sustainable, and green energy has become one of the vital tasks for researchers and scientists to address the rapidly increasing global warming and energy crises [1–3]. The energy harvesting devices from our living environment is an effective approach such as air, solar, wind, chemical, thermal, and mechanical energy and has attracted lots of research interests in the scientific community [4]. Among them, mechanical energy is one of the efficient approaches to provide a sustainable, green power source for self-powered devices such as portable/wearable electronics and wireless sensor network [5–10]. Up to now, a variety of approaches have been explored to convert mechanical energy to electrical energy utilizing electromagnetic [11], electrostatic [12], piezoelectric [13, 14], pyroelectric [15], and triboelectric effects [16–18].

Recently, triboelectric nanogenerators (TENGs) are considered a potential approach to generate electricity from mechanical energy via electrostatic induction and triboelectric charging [19–21]. Owing to its easy fabrication, cost-effectiveness, high output voltage, and high performance, it has broad potential applications, including self-powered sensors, health care monitoring, and portable electronic devices [22–25]. Although a variety of materials have been studied as active materials in TENG, it still has its limitations. So far, numerous approaches have been explored in TENG to achieve higher output performance, by choosing and varying the surface morphology of the materials. On the other hand, unique coupling of the piezoelectric materials with TENG is one of the promising approaches to
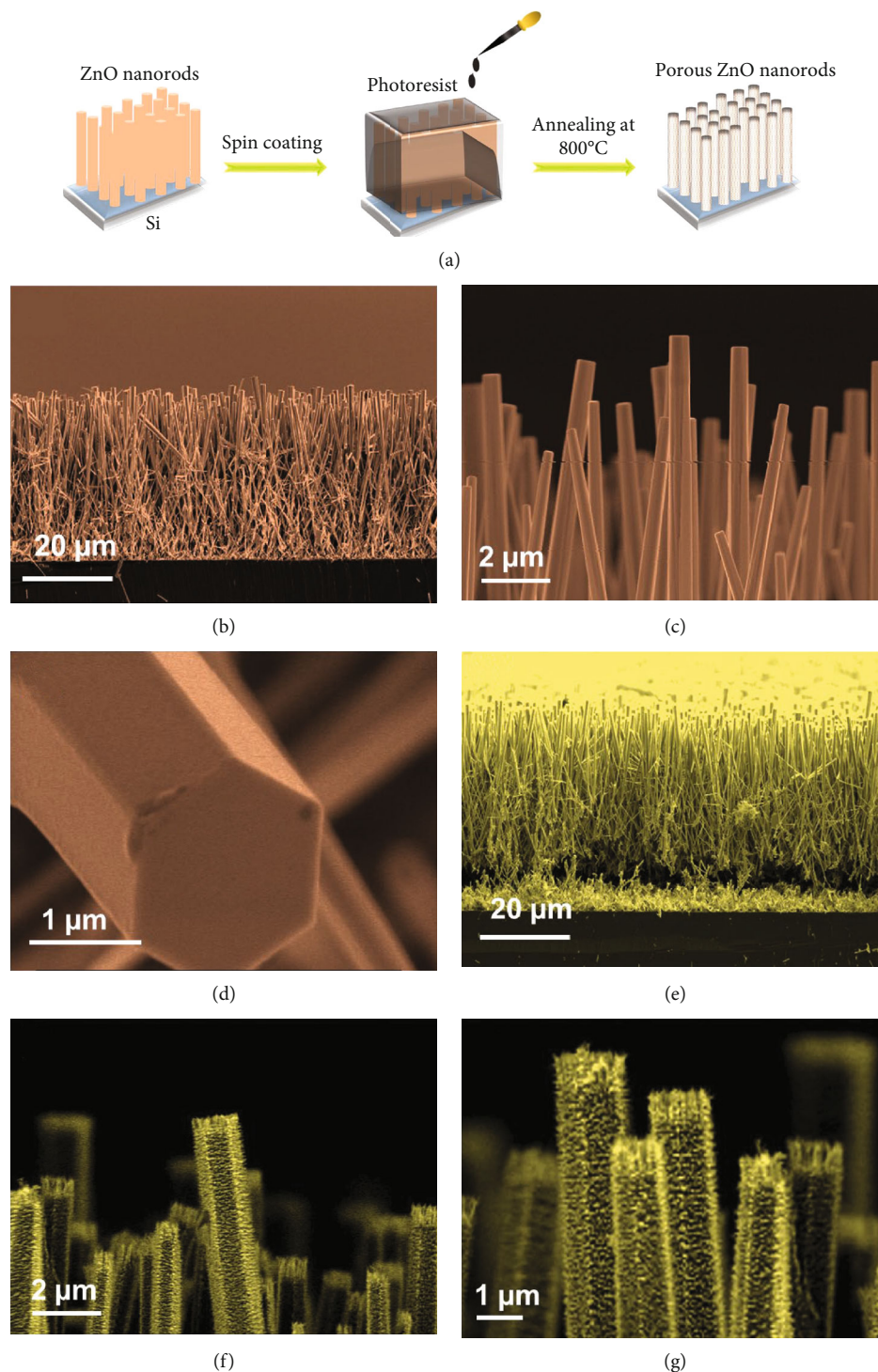
Figure 1: (a) Schematic representation process for the surface modification of ZnO nanorods. High- and low-magnification SEM images of (b–d) smooth ZnO NRs and (e–g) M: ZnO NRs.

greatly improve the electrical output performance [26–29]. However, identifying the piezoelectric materials with high relative permittivity and high piezoelectric coefficients is the key factor to increase the electrical performance of nanogenerators. Therefore, strenuous efforts have been devoted to fabricate and design a high-performance TENG for powering electronic systems.

Among various piezoelectric materials, ZnO has been considered a promising material for energy harvesting functions due to its relatively large piezoelectric coefficient, nontoxicity, and easy synthesis [30, 31]. The ZnO nanorods (NRs) proposed in this study have high utility due to their advantages of high optical properties, good reliability, and human-friendly stability [32]. Additionally, discrete surfaces

of ZnO NRs would be desirable for triboelectric nanogenerators which require an efficient contact and interface to the surface of triboelectric polymer materials.

Herein, we will first elucidate a simple method to introduce surface modification in ZnO nanorods (M: ZnO NRs) to porous nanofiber-like structures. The surface modification of ZnO nanorods to porous nanofibers is created by nanoetching the nanorods using a photoresist (PR) at 800°C. M: ZnO NR-based piezoelectric nanogenerators (PENG) were initially fabricated to verify the practical ability of the device for converting mechanical energy into electrical energy. Then, we fabricated triboelectric nanogenerators (TENG) using M: ZnO NRs encapsulated with poly (dimethylsiloxane) (PDMS) as negative triboelectric material and mica as positive triboelectric material. A strongly enhanced output voltage and current density are achieved in the case of M: ZnO NRs, when compared to smooth ZnO nanorods. We noted that the obtained output power was capable of lighting 24 commercial red emission light-emitting diodes (LEDs) connected in series without using any energy storage systems.

2. Experimental Section

2.1. Materials. Zn metal (99.999%), oxygen gas (99.999%), nitrogen gas (99.999%), and PR S-1813G® were purchased from Sigma-Aldrich.

2.2. Synthesis of ZnO and M: ZnO Nanorods. ZnO nanorods were grown via chemical vapor deposition (CVD) system used in previous studies [33]. In a typical ZnO nanorod growth experiment, high-purity zinc (Zn) metal contained in a quartz boat is placed in the center zone of the CVD chamber. Then, oxygen (200 sccm) was used as a source and carrier gas for the deposition of ZnO nanorods. The growth temperature of ZnO nanorods was set at 750°C for 40 min. For the production of surface-modified ZnO nanorods, PR S-1813G® and photoresist thinner were used. The equal ratio of photoresist (10 mL) and thinner was mixed thoroughly to make diluted PR. Then, the diluted PR was spin-coated on the ZnO NRs and heated up to 800°C for 30 min. The schematic representation of the surface modification of ZnO nanorods is illustrated in Figure 1(a). The details about the characterization, piezo, and triboelectric measurements are presented in the supporting information (SI (available here)).

3. Results and Discussions

The morphological characteristics of the as-prepared and surface-etched ZnO NRs were investigated by scanning electron microscope (SEM). Figures 1(b)–1(d) display the typical SEM images of as-prepared ZnO NRs on Si substrate using the CVD technique. As seen from the images, ZnO NRs appear to have a smooth surface with flattened hexagonal corners. The mean diameter of the ZnO NRs is about 1.5 μm and length up to 40 μm. Figures 1(e)–1(g) display the morphology change of the ZnO NRs after surface etching with PR for 800°C at 30 min. As can be seen from Figures 1(e)–1(g), the ZnO NRs with a hexagonal shape were
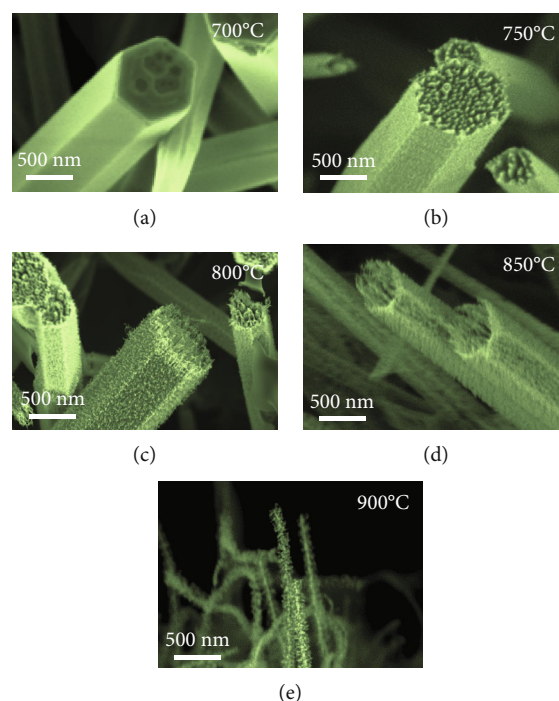

FIGURE 2: SEM image showing the etching dependence on thermal treatment of PR-coated ZnO NRs at (a) 700°C, (b) 750°C, (c) 800°C, (d) 850°C, and (e) 900°C.
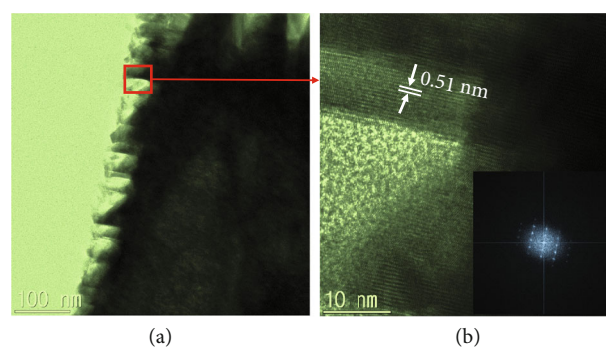

FIGURE 3: (a) TEM and (b) HRTEM image of M: ZnO NRs (inset shows FFT pattern).

found to possess nanofiber-like morphology after the thermal treatment. The surface etching of ZnO with PR results in strong texturing of the NRs. The morphology of ZnO NRs is strongly changed, and the smooth surface of ZnO NRs becomes coarse and rough. In order to understand the morphological change of ZnO NRs, we performed systematic studies by varying thermal treatment on PR-coated ZnO NRs at different temperatures. Figure 2 depicts SEM images of ZnO NRs after thermal treatment at different temperatures (700–900°C). Here, thermal treatment at 700°C has very little effect on the morphology of NRs with the side surface still smooth with little etching on the top of NRs (Figure 2(a)). When the temperature was elevated to 750°C, a change of surface texture on ZnO NR sidewalls was noticed, and a nanofiber-like structure appeared on
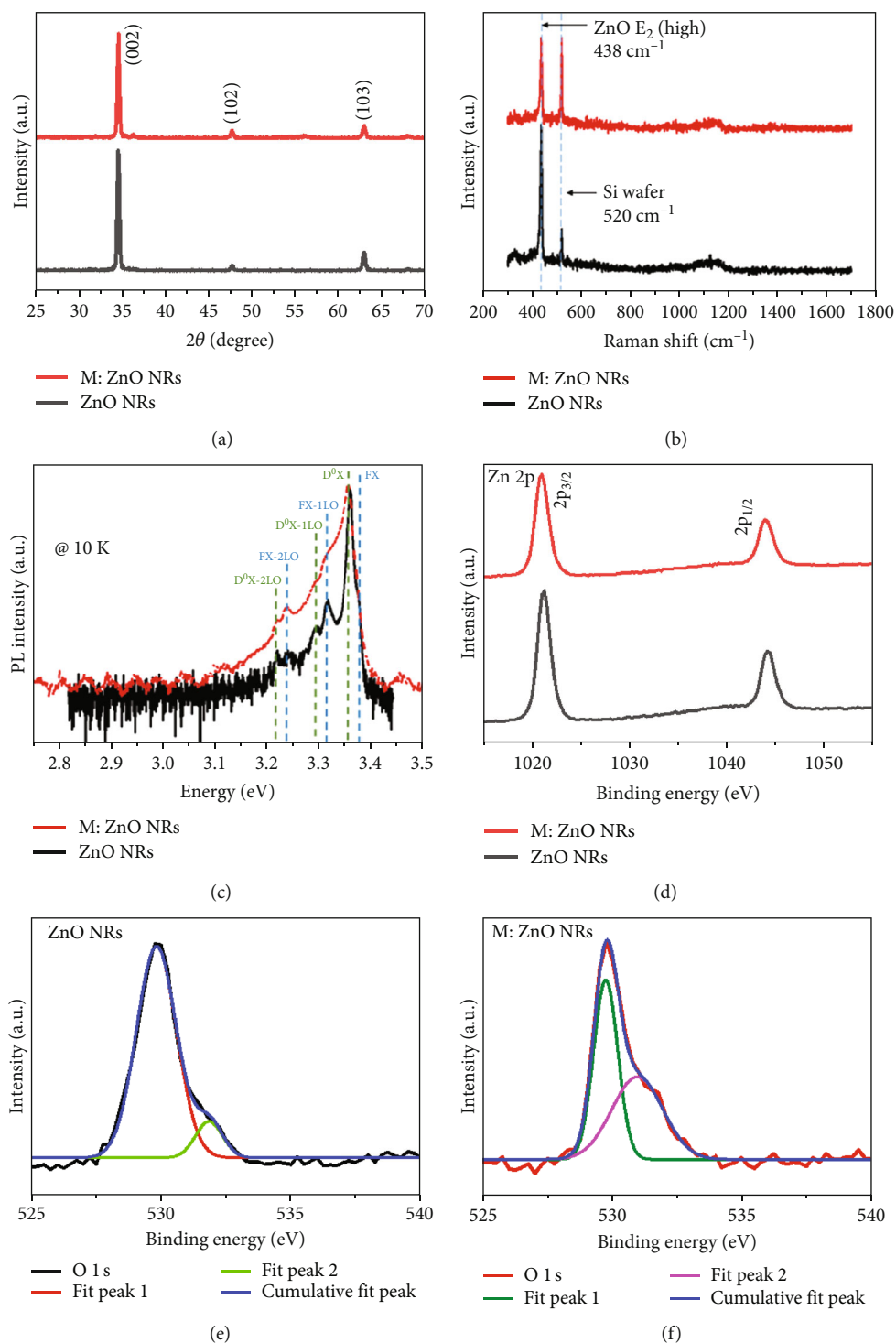
Figure 4: (a) XRD pattern of smooth ZnO NRs and M: ZnO NRs. (b) Raman spectrum of smooth ZnO NRs and M: ZnO NRs. (c) Low-temperature PL spectrum of smooth ZnO NRs and M: ZnO NRs. (d) XPS spectra of Zn 2p of smooth ZnO NRs and M: ZnO NRs. (e, f) XPS spectra of O 1s of smooth ZnO NRs and M: ZnO NRs.

the top of NRs indicating the beginning of a chemical attack (Figure 2(b)). The thermal treatment at 800°C caused major etching characteristics, with apparent change to the surface of ZnO NRs (Figure 2(c)). A nanofiber-like morphology

with sharp tips was observed on the top and sidewalls of the NRs. The nanofibers appear to penetrate almost through the whole NRs making it highly porous. These porous structures with defects thereby produce strain and enhance the
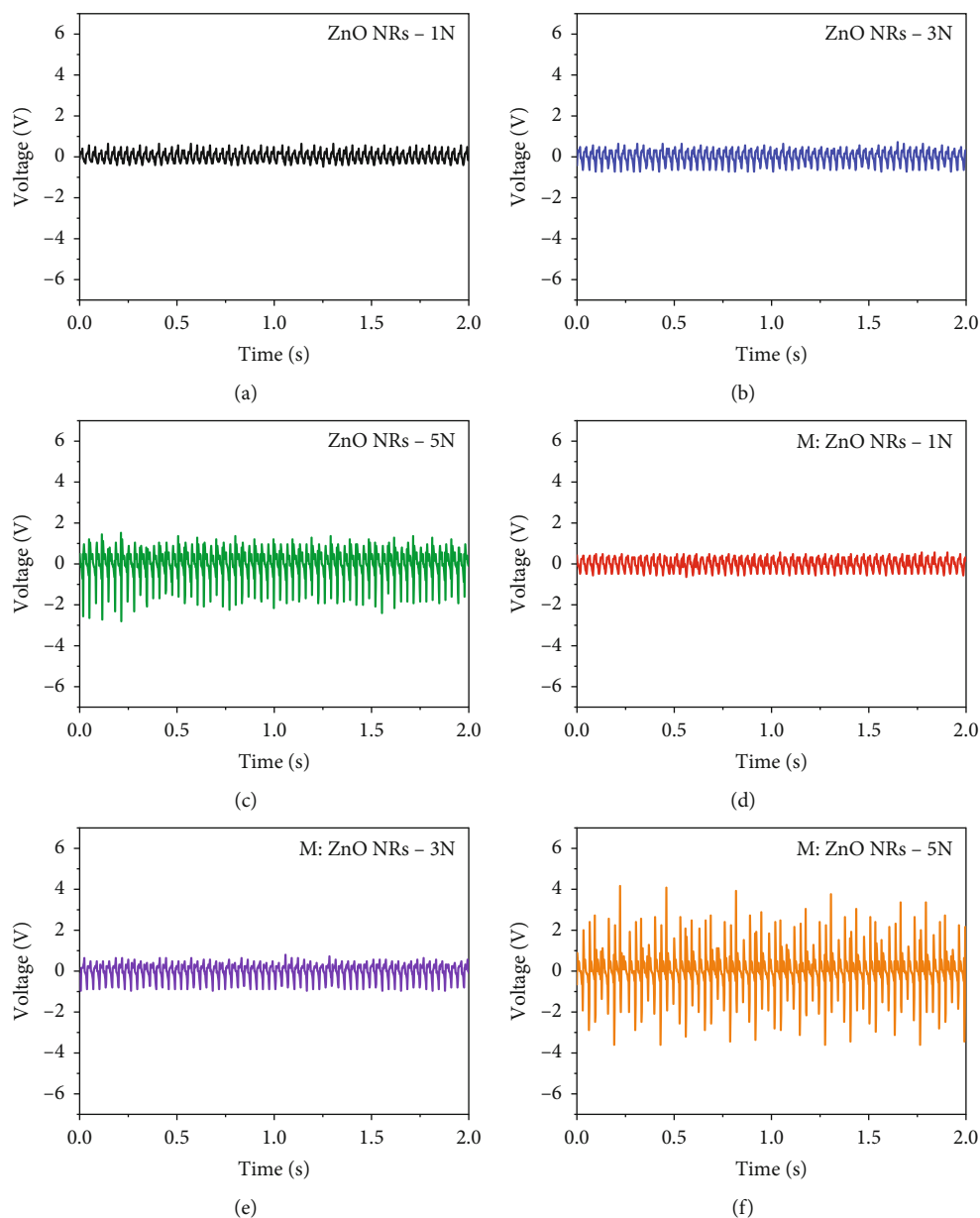
FIGURE 5: Peak-to-peak output voltage of (a–c) smooth ZnO NRs and (d, f) M: ZnO NRs under various compressive forces.

piezoelectric properties in surface-modified ZnO NRs (M: ZnO NRs). When the thermal treatment is prolonged above 850°C, there is more etching rate, and it brings significant morphological changes and damages the NRs (Figures 2(d) and 2(e)). Hence, we can conclude that nanofibers of ZnO NRs occur at 800°C under 30 min etching time.

To investigate the microstructure of M: ZnO NRs, high-resolution transmission electron microscopy (HRTEM) was employed. Figure 3(a) displays the typical TEM image of M: ZnO NRs. It should be noted here that fiber-like morphology becomes apparent, which agrees with SEM results. Figure 3(b) depicts an HRTEM image of M: ZnO NRs, where clear lattice fringes with a spacing of 0.51 nm correspond to (0001) planes of hexagonal ZnO. Furthermore, the fast Fourier transform (FFT) pattern (inset Figure 3(b)) confirms the good crystalline nature of M: ZnO NRs.

Additionally, the EDX spectrum was measured for both ZnO NRs and M: ZnO NRs (Figure S1), which confirms the peaks of Zn and oxygen elements in ZnO NRs.

The crystalline structures of the as-grown ZnO NRs and M: ZnO NRs were investigated using X-ray diffraction (XRD) and Raman spectroscopy. Figure 4(a) shows the corresponding diffraction patterns of ZnO NRs and M: ZnO NRs. The XRD patterns show a sharp peak at approximately 34.54°, corresponding to the (002) plane, indicating good alignment in the c-axis direction. Figure 4(b) displays the typical Raman spectra of smooth ZnO NRs and M: ZnO NR films. As seen from Figure 4(b), a dominant sharp peak positioned at 438 cm^{-1} was observed for smooth ZnO NRs, which is assigned to E_2 (high) vibration mode of wurtzite ZnO and is associated with the vibration of oxygen atoms [34, 35]. The presence of the strong intense E_2 (high) mode
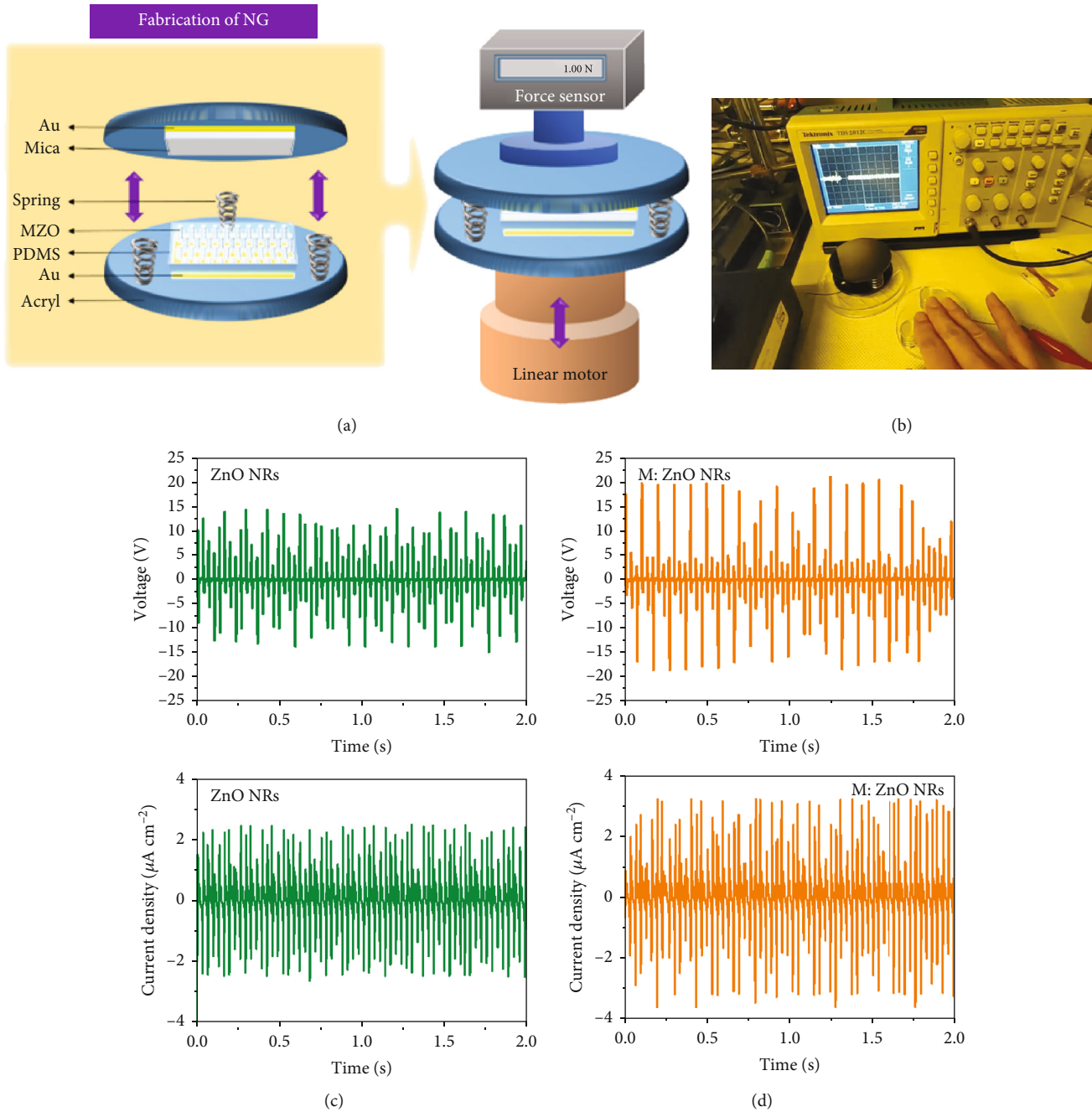
(a)

(b)

(c)

(d)

FIGURE 6: (a) Schematic illustration of the M: ZnO NR-based TENGs. (b) Photographic image of the output voltage generated from M: ZnO NR TENG during the external pushing force. (c) The output voltage and (d) current density of smooth ZnO NRs and M: ZnO NRs.

confirms the good crystallinity of the as-prepared smooth NRs. The Raman spectra of M: ZnO NRs were similar to that of smooth NRs. However, the peak intensity of the E_2 (high) mode decreased for M: ZnO NRs. This indicates that surface etching induces stress in ZnO NRs and decreases the intensities which was mainly caused by the chemical reaction of photoresist.

Low-temperature photoluminescence (PL) was then employed to study the optical properties of smooth ZnO NRs and M: ZnO NR films. Figure 4(c) illustrates PL results of smooth ZnO NRs and M: ZnO NR films obtained at 10 K.

As shown in the PL spectra, smooth ZnO NRs exhibit an emission band located at 3.378 eV (attributed to free exciton (FX) emission), which is consistent with other reports [36]. The emission centered at 3.36 eV is assigned to donor-bound exciton (D^0X), which dominates the NBE of smooth ZnO NRs. The emission centered at 3.310 and 3.238 eV is related with longitudinal optical (LO) phonon replicas of FX-1LO and FX-2LO, respectively. The energy difference between these two replicas is close to 72 meV, corresponding to the LO-phonon energy of ZnO [37]. Additionally, the shoulder peaks centered at 3.292 and 3.220 eV correspond
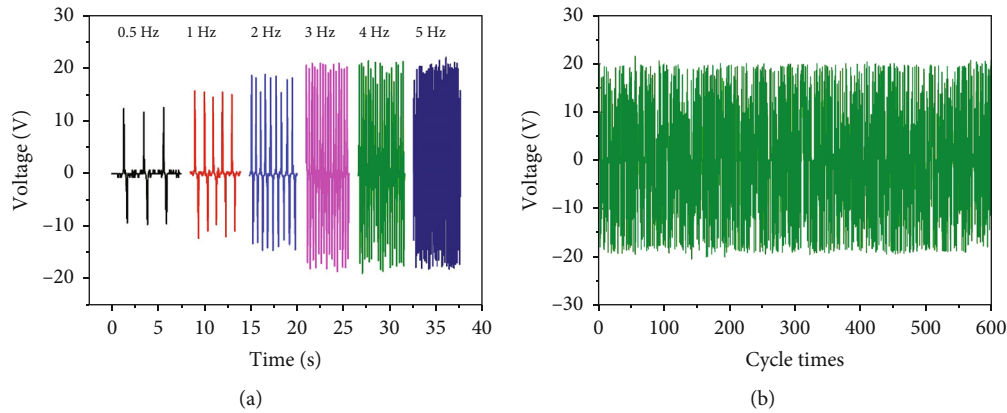
(a)

(b)

FIGURE 7: (a) Open-circuit voltages of M: ZnO NR TENG under different frequencies. (b) Stability of the proposed M: ZnO NR TENG device for 600 cycles.
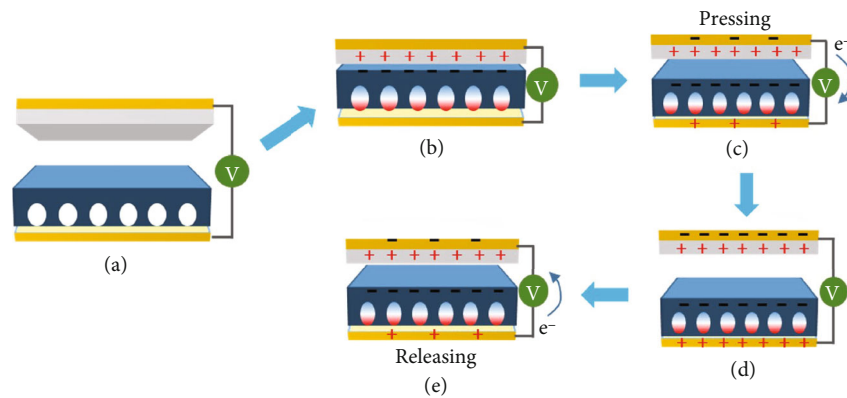

FIGURE 8: Schematic diagram for the working mechanism and charge generation of the M: ZnO NR TENGs.

to phonon replicas of D^0X–1LO and D^0X–2LO. The PL of M: ZnO NR films at 10 K is quite similar to that of smooth ZnO NRs. However, the PL intensity of M: ZnO NRs increases as compared to smooth ZnO NRs. The enhancement of PL intensity could be related with the reduction of dislocation and extraction of strong luminescence by light scattering from the sidewalls of the porous ZnO NRs [38].

XPS measurements were further carried out to study the surface states and chemical composition in ZnO NRs and M: ZnO NRs. The core level spectra of Zn 2p, for ZnO NRs and M: ZnO NRs, are displayed in Figure 4(d). The binding energies at 1020.24 eV (Zn $2p_{3/2}$) and 1044.07 eV (Zn $2p_{1/2}$) reveal the Zn^{2+} valence state in ZnO NRs and M: ZnO NRs [39]. Similarly, the spectra of O 1s were found to be deconvoluted into two peaks at 530.1 eV and 531.8 eV (Figures 4(e) and 4(f)). The peak at 530.1 eV is ascribed to O^{2-} ion on the wurtzite structure of ZnO, and the peak at 531.8 eV is ascribed to the loosely bound O^{2-} ions on ZnO surface such as hydroxyl OH groups [40].

Initially, we prepared the piezoelectric nanogenerator PENG devices on smooth ZnO NRs and M: ZnO NR film, to investigate their electrical properties under a periodic pushing force. We compared the peak-to-peak output voltage for the smooth ZnO NRs and M: ZnO NR film under different pushing forces (1, 3, and 5 N). As seen in Figure 5,

the output voltage for smooth ZnO NRs and M: ZnO NR film device increased gradually with the mechanical pushing force varying from 1 to 5 N. We observed that the effective output voltage measured for M: ZnO NR device (with a vertical force of 5 N) is 2 times higher than those obtained for smooth ZnO NR device (Figure 5(b)). The enhanced output voltage is due to the highly porous structure of NRs, which produces strain and enhances the piezoelectric potential in M: ZnO NRs [41, 42]. Additionally, the higher specific surface area of porous ZnO NRs is also significant in enhancing their piezoelectric response [43, 44].

A schematic representation of the M: ZnO NR-based TENG device is depicted in Figure 6(a). The typical process involved in the fabrication of TENG is described below. In the triboelectric series, mica and PDMS are excellent positive and negative materials, respectively [45]. For the positive layer, an Au electrode was deposited by e-beam evaporation on the backside of mica films prepared with dimensions of 1.5 cm × 1.5 cm. As for the negative layer, PDMS (SYL-GARD® 184, Dow Corning) was spin-coated (300 rpm) on M: ZnO nanorods, and Au electrodes were deposited on the backside. For comparison, a negative layer using bare ZnO nanorods was also fabricated. Each of the two layers was attached to two acrylic substrates, respectively, and fixed between the two layers with a spring. The fabricated TENG
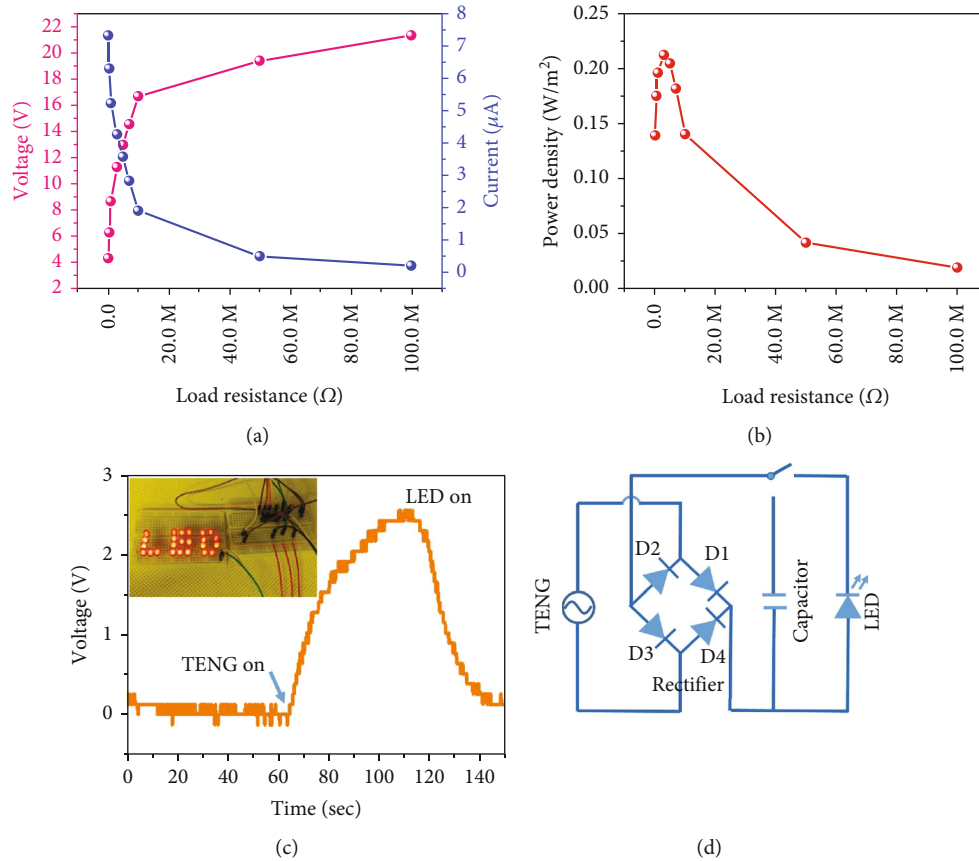
(a)

(b)

(c)

(d)

FIGURE 9: (a) Output voltage and current values of the M: ZnO NR TENG with various external load resistances. (b) Measured power density curves as a function of external load resistances. (c) The charging and discharging rectified voltage curve used to power up the LEDs using the M: ZnO NR TENG. The inset shows the photographic images of red color LEDs operated using the M: ZnO NR TENG device. (d) The corresponding equivalent electric circuit of the M: ZnO NR TENG-based self-charging system.

performed a contact-non-contact cycle by fixing a force gauge and a linear motor to both sides of the device for triboelectric generation. Figure 6(b) represents the photographic image of the output voltage generated from M: ZnO NR TENG during the external pushing force. The output voltage and current density of smooth ZnO NRs and M: ZnO NR TENG devices were systematically studied under a constant vertical force of 5 N. Figures 6(c) and 6(d) display the output voltage and current densities of smooth ZnO NRs and M: ZnO NRs. Here, the maximum output voltage and current density obtained for smooth ZnO NR TENG are noted to be 12 V and 2.5 μA cm^{-2}. However, the output voltage and current density for M: ZnO NR TENG increased to be 20 V and 3.2 μA cm^{-2}, which is higher than that of smooth ZnO NRs.

Besides, the output performances of M: ZnO NR TENG under the application of different frequencies were also investigated. The output voltage of the M: ZnO NR TENG measured at different applied frequencies ranging from 0.5 to 5 Hz at a constant applied external force of 5 N is shown in Figure 7(a). The measured output voltage of the M: ZnO NR TENG was slightly enhanced while increasing the frequency from 0.5 to 5 Hz. This improvement is mainly attributed to the faster compression cycles with an increase in frequency, which can lead to an increase in charge trans-

fer rate across the external load [29, 46]. To demonstrate the durability of the M: ZnO NR TENG device, continuous testing was carried out over 600 cycles (Figure 7(b)). The TENG device shows no noticeable degradation in the performance over 600 cycles demonstrating the excellent durability of our M: ZnO NR TENG device.

The plausible mechanism of the fabricated M: ZnO NR TENG is schematically depicted in Figure 8. At the initial stage, when there is no contact between the top (Au/mica) and the bottom (PDMS/M: ZnO NRs) surfaces, there is no electric output, and no charges are generated (Figure 8(a)). Under the application of mechanical force on the top electrode, the top (mica) and bottom (PDMS/M: ZnO NRs) surfaces come in contact with each other (Figure 8(b)) generating positive and negative triboelectric charges on mica and PDMS surface. Due to the triboelectric effect, electrons from the mica surface can be induced to migrate into the PDMS/M: ZnO NRs, resulting in positive triboelectric charges along the surface of the mica layer. At the same time, due to the porous structure, a piezoelectric potential is generated in the M: ZnO NRs when the device is compressed by this mechanical force. This piezoelectric potential established on the PDMS/M: ZnO NRs could then extract more electrons from the mica layer (Figure 8(c)). When releasing the mechanical force, both the electrode surfaces are
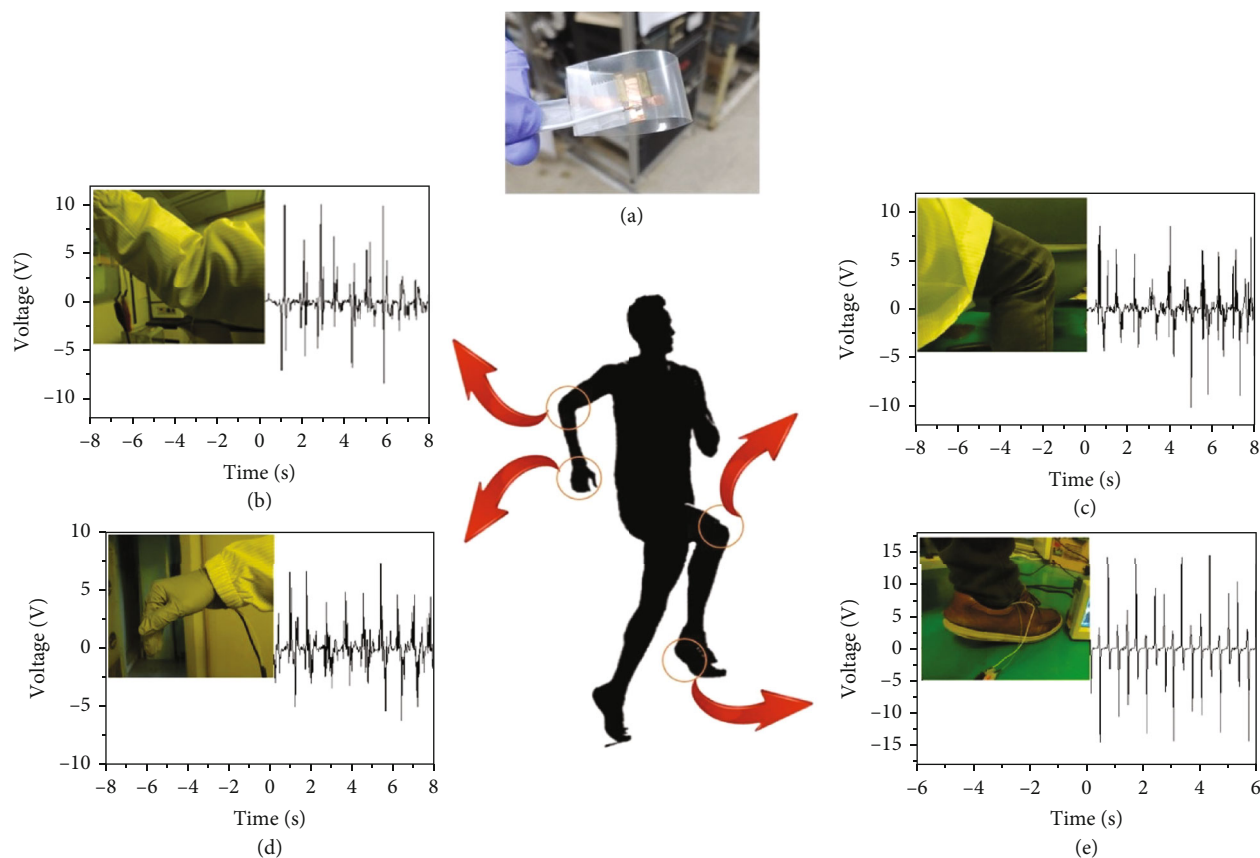
FIGURE 10: Real-time and practical applications of the TENG for harvesting mechanical energy from everyday human activities. (a) Photographic images and corresponding output electrical values of the TENG device attached to the (b) elbow, (c) knee, (d) wrist and (e) heel, respectively, during the running process.

separated from each other, which results in a potential difference between the two electrodes. This existing potential difference between the top and bottom electrodes drives the electrons to migrate from the bottom to top electrode via the external circuit (Figure 8(d)). This process results in the generation of positive peaks in current and voltage measurement. Once the mechanical force is processed again in the top electrode, the electrons will migrate back in the reverse direction to the bottom electrode, due to piezoelectric potential induced by the deformation of PDMS/M: ZnO NRs, which influences the triboelectric charges of the top electrode. This process generates negative peaks in current and voltage measurements (Figure 8(e)).

For practical applications of TENG, it is relevant to investigate the effective output power that the device can provide with a load. Therefore, the output voltage, current, and instantaneous power generated from the M: ZnO NR device were evaluated under several load resistances and are shown in Figure 9(a). The output voltage increases with an increasing load resistance while the output current decreases. The corresponding output power was calculated, and the maximum output power density of $21.3\,\mu W/cm^2$ was achieved with a $3\,M\Omega$ load resistance (Figure 9(b)). Finally, to demonstrate the practical applications of our as-prepared TENG device, we attempted to lit up multiple red emission LEDs. For this purpose, 24 LEDs constituting the

letter LED were connected to the TENG in series to a commercial bridge circuit. The output electrical power generated by the M: ZnO NRs is an alternating current (AC) signal and cannot be supplied directly to function electronic devices. Therefore, the AC signals generated were converted into direct current (DC) by utilizing a bridge rectifier. The output voltage generated from the M: ZnO NR TENG using a bridge rectifier is shown in Figure 8(c). Further, upon applying the external force by pressing, the prepared M: ZnO NR TENG device instantaneously and simultaneously powered 24 LEDs displaying the letters LED as shown in the inset of Figure 9(c). The corresponding equivalent circuit of the M: ZnO NR TENG-based self-charging system is shown in Figure 9(d).

We fabricated a TENG for actual testing and checked the voltage that can be spontaneously generated during the running process. Figure 10(a) shows a test TENG with a $1.5 \times 1.5\,cm$ size. The mica positive layer and the PDMS+M: ZnO negative layer were fabricated to enable contact and noncontact cycles without a spring by using a PET substrate with strong flexibility. Figures 10(b)–10(e) and the photographic image (Figure S2 Supporting Information) display the results of experiments by attaching TENG to the elbow, knee, wrist, and heel, respectively. Since the joint part of the human body that folds receives relatively little force, a small voltage of about 5 to 7 V is generated, and

the results of the heel test that can be used with self-powered shoes are similar to those using a linear motor. The above experimental results clearly demonstrate the excellent performance of M: ZnO NR TENG for their potential application for energy harvesting structure for self-powered devices.

4. Conclusions

In summary, we successfully modified the surface of the single-crystal hexagonal ZnO nanorods using PR as an etching source. The structural analysis shows that the surface-modified ZnO NRs exhibited nanofiber-like porous structure and possessed high surface-to-volume ratios. To clearly examine the advantage of the surface modification, TENG devices were fabricated on M: ZnO NRs. The devices exhibit an output voltage of 20 V and a current density of $3.2\,\mu\text{A}\,\text{cm}^{-2}$ under a constant vertical force of 5 N. The M: ZnO NR TENG device can be able to lit 24 red LEDs as a power source. The practical application of M: ZnO NR TENG was also verified by fixing it onto the shoes, and the electrical output performances by various human activities were observed, verifying that the proposed device can efficiently harvest these energies. The results highlight the potential of M: ZnO NR TENG devices for energy harvesting structure for self-powered devices.

Data Availability

The data used to support the findings of this study included within the article and supporting information are available from the corresponding author upon reasonable request.

Conflicts of Interest

The authors declare no conflict of interest.

Acknowledgments

Supplementary Materials

TEM and EDX spectra of smooth ZnO and M: ZnO NRs. A photographic image file represents the output electrical energy generated from the harvesting of mechanical energy by using a TENG during various human body activities (running), respectively. (Supplementary Materials)

References

[1] Z. L. Wang, "Triboelectric nanogenerators as new energy technology for self-powered systems and as active mechanical and chemical sensors," *ACS Nano*, vol. 7, no. 11, pp. 9533–9557, 2013.

[2] M. Lee, J. Bae, J. Lee, C.-S. Lee, S. Hong, and Z. L. Wang, "Self-powered environmental sensor system driven by nanogenera-

tors," *Energy & Environmental Science*, vol. 4, no. 9, pp. 3359–3363, 2011.

[3] Y. Yang, S. Wang, Y. Zhang, and Z. L. Wang, "Pyroelectric nanogenerators for driving wireless sensors," *Nano Letters*, vol. 12, no. 12, pp. 6408–6413, 2012.

[4] D. Jiang, B. Shi, H. Ouyang, Y. Fan, Z. L. Wang, and Z. Li, "Emerging implantable energy harvesters and self-powered implantable medical electronics," *ACS Nano*, vol. 14, no. 6, pp. 6436–6448, 2020.

[5] Y. Zou, V. Raveendran, and J. Chen, "Wearable triboelectric nanogenerators for biomechanical energy harvesting," *Nano Energy*, vol. 77, article 105303, 2020.

[6] S. A. Graham, S. C. Chandrarathna, H. Patnam, P. Manchi, J.-W. Lee, and J. S. Yu, ""Harsh environment–tolerant and robust triboelectric nanogenerators for mechanical-energy harvesting", sensing, and energy storage in a smart home," *Nano Energy*, vol. 80, article 105547, 2021.

[7] B. Dudem, R. I. G. Dharmasena, S. A. Graham et al., "Exploring the theoretical and experimental optimization of high-performance triboelectric nanogenerators using micro-architectured silk cocoon films," *Nano Energy*, vol. 74, article 104882, 2020.

[8] Q. Zheng, H. Zhang, B. Shi et al., "In vivo self-powered wireless cardiac monitoring via implantable triboelectric nanogenerator," *ACS Nano*, vol. 10, no. 7, pp. 6510–6518, 2016.

[9] W. He, H. Van Ngoc, Y. T. Qian et al., "Synthesis of ultra-thin tellurium nanoflakes on textiles for high-performance flexible and wearable nanogenerators," *Applied Surface Science*, vol. 392, pp. 1055–1061, 2017.

[10] Z. Wen, M.-H. Yeh, H. Guo et al., "Self-powered textile for wearable electronics by hybridizing fiber-shaped nanogenerators, solar cells, and supercapacitors," *Science Advances*, vol. 2, no. 10, article e1600097, 2016.

[11] S. Roundy and E. Takahashi, "A planar electromagnetic energy harvesting transducer using a multi-pole magnetic plate," *Sensors and Actuators, A: Physical*, vol. 195, pp. 98–104, 2013.

[12] H. Tian, S. Ma, H.-M. Zhao et al., "Flexible electrostatic nanogenerator using graphene oxide film," *Nanoscale*, vol. 5, no. 19, pp. 8951–8957, 2013.

[13] W. Wu, L. Wang, Y. Li et al., "Piezoelectricity of single-atomic-layer MoS_2 for energy conversion and piezotronics," *Nature*, vol. 514, no. 7523, pp. 470–474, 2014.

[14] Y. Qian and D. J. Kang, "Poly(dimethylsiloxane)/ZnO nano-flakes/three-dimensional graphene heterostructures for high-performance flexible energy harvesters with simultaneous piezoelectric and triboelectric generation," *ACS Applied Materials & Interfaces*, vol. 10, no. 38, pp. 32281–32288, 2018.

[15] Y. Yang, W. Guo, K. C. Pradel et al., "Pyroelectric nanogenerators for harvesting thermoelectric energy," *Nano Letters*, vol. 12, no. 6, pp. 2833–2838, 2012.

[16] Y. Jie, J. Ma, Y. Chen, X. Cao, N. Wang, and Z. L. Wang, "Efficient delivery of power generated by a rotating triboelectric nanogenerator by conjunction of wired and wireless transmissions using Maxwell's displacement currents," *Advanced Energy Materials*, vol. 8, no. 31, article 1802084, 2018.

[17] C. Zhang, J. Chen, W. Xuan et al., "Conjunction of triboelectric nanogenerator with induction coils as wireless power sources and self-powered wireless sensors," *Nature Communications*, vol. 11, no. 1, p. 58, 2020.

[18] Z. Haider, A. Haleem, R. Shan Ahmad et al., "Highly porous polymer cryogel based tribopositive material for high performance

triboelectric nanogenerators," *Nano Energy*, vol. 68, article 104294, 2020.

[19] Y. Shi, F. Wang, J. Tian et al., "Self-powered electro-tactile system for virtual tactile experiences," *Science Advances*, vol. 7, no. 6, article eabe2943, 2021.

[20] A. Haleem, J.-M. Pan, A. Shah, H. Hussain, and W.-D. He, "A systematic review on new advancement and assessment of emerging polymeric cryogels for environmental sustainability and energy production," *Separation and Purification Technology*, vol. 316, article 123678, 2023.

[21] A. Haleem, Z. Haider, R. Shan Ahmad et al., "Highly porous and thermally stable tribopositive hybrid bimetallic cryogel to boost up the performance of triboelectric nanogenerators," *International Journal of Energy Research*, vol. 44, no. 11, pp. 8442–8454, 2020.

[22] S. Parandeh, M. Kharaziha, and F. Karimzadeh, "An eco-friendly triboelectric hybrid nanogenerators based on graphene oxide incorporated polycaprolactone fibers and cellulose paper," *Nano Energy*, vol. 59, pp. 412–421, 2019.

[23] L. Dhakar, S. Gudla, X. Shan et al., "Large scale triboelectric nanogenerator and self-powered pressure sensor array using low cost roll-to-roll UV embossing," *Scientific Reports*, vol. 6, no. 1, article 22253, 2016.

[24] R. Shan Ahmad, A. Haleem, Z. Haider et al., "Realizing the capability of negatively charged graphene oxide in the presence of conducting polyaniline for performance enhancement of tribopositive material of triboelectric nanogenerator," *Advanced Electronic Materials*, vol. 6, no. 5, article 2000034, 2020.

[25] P. Claver Uzabakiriho, Z. Haider, K. Emmanuel et al., "High-performance, mechanically and thermally compliant silica-based solid polymer electrolyte for triboelectric nanogenerators application," *Advanced Materials Technologies*, vol. 5, no. 7, article 2000303, 2020.

[26] S. Chen, X. Tao, W. Zeng, B. Yang, and S. Shang, "Quantifying energy harvested from contact-mode hybrid nanogenerators with cascaded piezoelectric and triboelectric units," *Advanced Energy Materials*, vol. 7, no. 5, article 1601569, 2017.

[27] X. Chen, M. Han, H. Chen et al., "A wave-shaped hybrid piezoelectric and triboelectric nanogenerator based on P(VDF-TrFE) nanofibers," *Nanoscale*, vol. 9, no. 3, pp. 1263–1270, 2017.

[28] P. Manchi, S. A. Graham, H. Patnam, M. V. Paranjape, and J. S. Yu, "rGO-ZnSnO3 nanostructure-embedded triboelectric polymer-based hybridized nanogenerators," *Advanced Materials Technologies*, vol. 7, no. 8, article 2101460, 2022.

[29] P. Manchi, S. A. Graham, H. Patnam, M. V. Paranjape, and J. S. Yu, "ZnO nanoflakes embedded polymer matrix for high-performance mechanical energy harvesting," *Advanced Materials Technologies*, vol. 7, no. 3, article 2100858, 2022.

[30] Q. He, X. Li, J. Zhang, H. Zhang, and J. Briscoe, "P–N junction-based ZnO wearable textile nanogenerator for biomechanical energy harvesting," *Nano Energy*, vol. 85, article 105938, 2021.

[31] C. Jirayupat, W. Wongwiriyapan, P. Kasamechonchung et al., "Piezoelectric-induced triboelectric hybrid nanogenerators based on the ZnO nanowire layer decorated on the Au/polydimethylsiloxane–Al structure for enhanced triboelectric performance," *ACS Applied Materials & Interfaces*, vol. 10, no. 7, pp. 6433–6440, 2018.

[32] Y. P. Jeon, J. H. Park, and T. W. Kim, "Highly-enhanced triboelectric nanogenerators based on zinc-oxide nanoripples act-

[33] S. R. Ryu, S. D. Gopal Ram, H.-D. Cho, D. J. Lee, T. W. Kang, and Y. Woo, "Single ZnO nanocactus gas sensor formed by etching of ZnO nanorod," *Nanoscale*, vol. 7, no. 25, pp. 11115–11122, 2015.

[34] D. J. Lee, S. R. Ryu, G. Mohan Kumar et al., "Enhanced UV photodetectivity in solution driven ZnO nanosheets via piezo-phototronic effect," *Journal of Materials Research and Technology*, vol. 13, pp. 397–407, 2021.

[35] G. Mohan Kumar, P. Ilanchezhiyan, A. Madhan Kumar, S. U. Yuldashev, and T. W. Kang, "Electrical property studies on chemically processed polypyrolle/aluminum doped ZnO based hybrid heterostructures," *Chemical Physics Letters*, vol. 649, pp. 130–134, 2016.

[36] H. He, Q. Yang, C. Liu, L. Sun, and Z. Ye, "Size-dependent surface effects on the photoluminescence in ZnO nanorods," *Journal of Physical Chemistry C*, vol. 115, no. 1, pp. 58–64, 2011.

[37] J. Zhou, K. Nomenyo, C. C. Cesar et al., "Giant defect emission enhancement from ZnO nanowires through desulfurization process," *Scientific Reports*, vol. 10, no. 1, p. 4237, 2020.

[38] J. Yu, L. Zhang, J. Shen, Z. Xiu, and S. Liu, "Wafer-scale porous GaN single crystal substrates and their application in energy storage," *CrystEngComm*, vol. 18, no. 27, pp. 5149–5154, 2016.

[39] Y. Qian, J. Yu, F. Zhang, Y. Kang, C. Su, and H. Pang, "Facile synthesis of sub-10 nm ZnS/ZnO nanoflakes for high-performance flexible triboelectric nanogenerators," *Nano Energy*, vol. 88, article 106256, 2021.

[40] P. Ilanchezhiyan, G. Mohan Kumar, F. Xiao et al., "Interfacial charge transfer in ZnTe/ZnO nano arrayed heterostructures and their improved photoelectronic properties," *Solar Energy Materials and Solar Cells*, vol. 183, pp. 73–81, 2018.

[41] Y. L. Su, K. Gupta, Y. L. Hsiao, R. C. Wang, and C. P. Liu, "Gigantic enhancement of electricity generation in piezoelectric semiconductors by creating pores as a universal approach," *Energy & Environmental Science*, vol. 12, no. 1, pp. 410–417, 2019.

[42] P.-C. Lee, Y.-L. Hsiao, J. Dutta, R.-C. Wang, S.-W. Tseng, and C.-P. Liu, "Development of porous ZnO thin films for enhancing piezoelectric nanogenerators and force sensors," *Nano Energy*, vol. 82, article 105702, 2021.

[43] H. V. Ngoc and D. J. Kang, "Flexible, transparent and exceptionally high power output nanogenerators based on ultrathin ZnO nanoflakes," *Nanoscale*, vol. 8, no. 9, pp. 5059–5066, 2016.

[44] Z. Yan and L. Y. Jiang, "Surface effects on the vibration and buckling of piezoelectric nanoplates," *Europhysics Letters*, vol. 99, no. 2, article 27007, 2012.

[45] X. Wang, W. Tong, Y. Li et al., "Mica-based triboelectric nanogenerators for energy harvesting," *Applied Clay Science*, vol. 215, article 106330, 2021.

[46] K. Shi, H. Zou, B. Sun, P. Jiang, J. He, and X. Huang, "Dielectric modulated cellulose paper/PDMS-based triboelectric nanogenerators for wireless transmission and electropolymerization applications," *Advanced Functional Materials*, vol. 30, no. 4, article 1904536, 2020.